Received: 22 February 2023 | Revised: 28 April 2023 | Accepted: 16 May 2023

DOI: 10.1002/jbm.a.37575

RESEARCH ARTICLE

Society For Biomaterials | WILEY

Antibacterial properties and osteoblast interactions of microfluidically synthesized chitosan – SPION composite nanoparticles

Melisa Kafali[1] | O. Berkay Şahinoğlu[2] | Yiğithan Tufan[1] | Z. Cemre Orsel[1] | Elif Aygun[3,4] | Beril Alyuz[3,4] | Emine Ulku Saritas[3,4,5] | E. Yegan Erdem[2,6] | Batur Ercan[1,7,8]

[1]Department of Metallurgical and Materials Engineering, Middle East Technical University, Ankara, Turkey

[2]Department of Mechanical Engineering, Bilkent University, Ankara, Turkey

[3]Department of Electrical and Electronics Engineering, Bilkent University, Ankara, Turkey

[4]National Magnetic Resonance Research Center (UMRAM), Bilkent University, Ankara, Turkey

[5]Neuroscience Graduate Program, Bilkent University, Ankara, Turkey

[6]National Nanotechnology Research Center (UNAM), Bilkent University, Ankara, Turkey

[7]BIOMATEN, Center of Excellence in Biomaterials and Tissue Engineering, Middle East Technical University, Ankara, Turkey

[8]Biomedical Engineering Program, Middle East Technical University, Ankara, Turkey

Correspondence
Batur Ercan, Department of Metallurgical and Materials Engineering, Middle East Technical University, 06800 Çankaya, Ankara, Turkey.
Email: baercan@metu.edu.tr

Funding information
The Scientific Research Council of Turkey, Grant/Award Numbers: 219M480, 118M652, 117M187; TÜBA (Outstanding Young Scientists Award, GEBİP) and Bilim Akademisi (Science Academy's Young Scientist Awards Program)

Abstract

In this research, a multi-step microfluidic reactor was used to fabricate chitosan – superparamagnetic iron oxide composite nanoparticles (Ch – SPIONs), where composite formation using chitosan was aimed to provide antibacterial property and nanoparticle stability for magnetic resonance imaging (MRI). Monodispersed Ch – SPIONs had an average particle size of 8.8 ± 1.2 nm with a magnetization value of 32.0 emu/g. Ch – SPIONs could be used as an MRI contrast agent by shortening T_2 relaxation parameter of the surrounding environment, as measured on a 3 T MRI scanner. In addition, Ch – SPIONs with concentrations less than 1 g/L promoted bone cell (osteoblast) viability up to 7 days of culture in vitro in the presence of 0.4 T external static magnetic field. These nanoparticles were also tested against *Staphylococcus aureus* (*S. aureus*) and *Pseudomonas aeruginosa* (*P. aeruginosa*), which are dangerous pathogens that cause infection in tissues and biomedical devices. Upon interaction of Ch – SPIONs with *S. aureus* and *P. aeruginosa* at 0.01 g/L concentration, nearly a 2-fold reduction in the number of colonies was observed for both bacteria strains at 48 h of culture. Results cumulatively showed that Ch – SPIONs were potential candidates as a cytocompatible and antibacterial agent that can be targeted to biofilm and imaged using an MRI.

KEYWORDS
antibacterial, magnetic field, microfluidics, osteoblast, SPION

1 | INTRODUCTION

Superparamagnetic iron oxide nanoparticles (SPIONs) have a great potential in both diagnostic and therapeutic applications due to their unique physical characteristics, such that their nanometric size provides large surface area to mass ratio, their surfaces can be easily modified due to having a negative surface charge, their superparamagnetic behavior allows high magnetic susceptibility, and they avoid clogging due to the absence of any retaining residual magnetism.[1–3] Additionally, SPIONs play a crucial role as contrast agents due to the changes they impart in the MRI relaxation of nearby spins. SPIONs can enhance MRI contrast by shortening longitudinal (T_1) and transverse (T_2) relaxations of the surrounding spins,[4] and based on their size and magnetization, SPIONs can be used as a dual contrast agent (T_1/T_2 relaxation).[5] Inside the body, the endogenous iron metabolic processes can breakdown and eliminate SPIONs from circulation. In fact, the iron produced by SPIONs can be processed in the liver, and then utilized in the production of red blood cells or eliminated through the kidneys.[6] The clearance time of SPIONs can vary according to their size, charge and injected dose, however, the average clearance time of SPIONs is 3–7 weeks following intravascular administration.[7] In addition, SPIONs are also shown to exhibit antibacterial properties against both gram negative and gram positive bacteria strains,[8] and successfully eradicate biofilms.[9] In fact, SPIONs are proposed as antibacterial agents even against strains that developed antibacterial resistance, that is, Methicillin Resistant *Staphylococcus aureus* (MRSA).[10] Importantly, the superparamagnetic nature of SPIONs allows them to be targeted under magnetic guidance; and therefore, enabled localization of the nanoparticles to the infected area in clinical applications.[11]

Despite the numerous advantages SPIONs offer, their cytotoxicity remains to be a critical issue. In literature, SPIONs were identified to generate oxidative stress, which was correlated with cell injury and death.[6] In fact, SPIONs were shown to decrease viability of L929 cells in a concentration-dependent manner up to 3 days in vitro.[12] One approach to remedy the toxicity issues of SPIONs is to coat them with organic acids and polymers.[13] Ghosh et al. showed that didodecylammonium bromide modified PLGA encapsulated SPIONs had lower toxicity towards human lymphocytes compared to their uncoated counterparts.[14] Park et al. also demonstrated that catechol functionalized polypeptide coated SPIONs did not show any toxicity towards human mesenchymal stem cells and had a minimal impact on cellular differentiation.[15] Aside from decreasing cytotoxicity, coating of SPIONs was also shown to increase their dispersibility, colloidal stability, and blood circulation time, which are all crucial factors for successful targeting of the magnetic nanoparticles to desired location in the body, that is, infected bone.[16] Being a biodegradable and biocompatible polymer, chitosan is a promising alternative to fabricate composite nanoparticles with SPIONs. Chitosan provides antibacterial activity with its positively charged amino groups by attacking the negatively charged bacterial cell wall.[17] In fact, chitosan cinnamaldehyde nanoparticles were observed to decrease *S. aureus* growth by 98% and *Escherichia coli* (*E. coli*) growth by 96%.[18]

There are various techniques in literature used to synthesize SPIONs, including chemical co-precipitation, micro-emulsions, hydrothermal synthesis and so on.[19] Among them, microfluidic systems provide a homogeneous reaction environment, efficient heat and mass transfer, controlled kinetic parameters and decreased chemical consumption, and therefore, lead to a controlled and monodisperse particle size distribution.[20] In addition, microfluidic devices have a small Reynolds number, and thus, they operate under laminar flow conditions,[13] which allows control over nucleation and growth kinetics during synthesis of SPIONs.[21] Microfluidic synthesis of SPIONs provides spherical shaped, high-quality, monodispersed particles, where alternate synthesis routes, that is, batch synthesis, failed to generate.[22] Frenz et al. observed that microfluidically synthesized SPIONs had a monocrystalline structure without any stacking faults and exhibited characteristic spinel crystal structure.[23] Ahrberg et al. showed that mean particle size of SPIONs synthesized with conventional batch process and microfluidic process were similar, however, the conventional batch process yielded a wider size distribution ($\sigma_{batch} = 2.4 \pm 0.27$ nm) compared to the microfluidically synthesized particles ($\sigma_{droplet} = 1.8 \pm 0.11$ nm).[24] We recently introduced a multistep microfluidic synthesis route for in situ coating of SPIONs with chitosan.[25] Though we proposed these nanoparticles for biomedical applications, the biological properties of SPIONs synthesized via the microfluidics approach has yet to be investigated.

In this study, antibacterial activity of microfluidically synthesized chitosan – SPION composite nanoparticles were investigated and their potential use as an MRI contrast agent was explored. Currently, the SPIONs approved by FDA for MRI monitoring have a limited use only in diagnostics.[7] However, composite nanoparticle fabrication of SPIONs with chitosan would provide further functionality to the SPIONs and potentially allow targeting, monitoring and enhanced antibacterial activity at the infection foci, that is, osteomyelitis. Towards this goal, we assessed the cytocompatibility of chitosan – SPION composite nanoparticles using osteoblasts (bone cells) in the absence and the presence of external static magnetic field. The antibacterial activity of nanoparticles was tested against *S. aureus* and *P. aeruginosa* biofilms, both of which are the leading causes of bone tissue and medical device-related infection.

2 | MATERIALS AND METHODS

All chemicals used in this work were analytical grade. Chitosan (50–190 kDa, 75%–85% deacetylated), ferric chloride hexahydrate ($FeCl_3.6H_2O$), ferrous chloride tetrahydrate ($FeCl_2.4H_2O$), acetic acid, ammonia (28%) and silicon oil were purchased from Sigma Aldrich. PDMS (polydimethylsiloxane) was obtained from Sylgard 184. SU-82005 negative photoresists were obtained from Microresist. Syringe with needle (10 mL) and tubing was purchased from ISOLAB. Dulbecco's Modified Eagle Medium (DMEM), penicillin–streptomycin, fetal bovine serum (FBS) and trypsin–EDTA were purchased from Biological Industries. 3 – (4,5-dimethyl-2-thiazolyl)-2,5-diphenyl-2H-tetrazolium bromide (MTT) was purchased from Abcam. Dimethyl

sulfoxide (DMSO), and hexamethyldisilazane were purchased from Sigma Aldrich. Tryptic Soy Broth (TSB) and agar were purchased from Merck.

2.1 | Device fabrication

Microfluidic channels were fabricated in polydimethylsiloxane (PDMS) using soft-lithography technique. Negative photoresist SU – 8 was used to prepare a master mold. PDMS was cast on the mold and cured at 80°C to form microfluidic channels. Afterwards, PDMS was bonded onto a glass slide using oxygen plasma. Finally, capillary tubing was fitted using epoxy to deliver the reagents.

2.2 | Particle synthesis

The synthesis route of nanoparticles was demonstrated in a previous study where a similar microfluidic reactor was utilized.[25] Briefly, SPIONs were synthesized using iron salt solution (1.09 g Fe (III) Chloride and 0.4 g Fe (II) Chloride in 100 mL distilled water, introduced from inlet 1 and 2) and ammonia solution (14% [v/v], introduced from inlet 3). For the synthesis of Ch – SPIONs, a chitosan solution (0.75 g chitosan was dissolved in 100 mL 0.3% [v/v] acetic acid, introduced from inlet 2) was prepared, while iron and ammonia solution concentrations were kept constant (introduced from inlet 1 and inlet 3, respectively). Silicon oil was used as the continuous phase to optimize flow configuration.

The solutions were introduced to the microchannels using syringe pumps (New Era NE-1000) at controlled flow rates. Since the prepared chitosan solution had a higher viscosity than the iron solution, chitosan solution was diluted with distilled water to obtain similar droplet volumes inside the channel.[26] The volumetric ratio of iron solution to chitosan solution was adjusted to be 1 to 1 to provide control on mixing of droplets. Silicon oil was delivered at a flow rate of 6.2 μL/min as the carrier fluid, iron salt solution and chitosan solution were supplied into the device at a rate of 3.1 μL/min as dispersed phases and ammonia solution was supplied into the device at a rate of 2.2 μL/min to initiate the co-precipitation reaction. The configuration of the device led to the generation of alternating droplets from the two solutions. The droplet formation process was monitored using an inverted microscope.

2.3 | Material characterization

Particles were imaged using FEI Nova Nano SEM 430 microscope. 20 kV accelerating voltage was employed during image procurement. Prior to SEM imaging, a thin layer of gold coating was applied onto the samples using Quorum SC7640 high-resolution sputter coater. Internal structure of the nanoparticles was investigated using high contrast transmission electron microscope (CTEM, FEI TECNAI F30) in bright field and selected area diffraction (SAED) modes. Size distribution of composite nanoparticles were determined by measuring 250 nanoparticles per sample using image processing software ImageJ. Crystallographic information of the nanoparticles was obtained using Rigaku D/Max-2200 X-ray diffractometer with monochromatic Cu Kα radiation at 40 kV. Diffraction angles (2θ) from 10° to 90° were scanned at 2°/min scanning rate, and the average of three experiments was taken for XRD spectra. Chemical analyzes were performed using Perkin Elmer 400 Fourier transform infrared (FTIR) spectrometer preparing KBr pellets. The scanning range was 4000–400 cm^{-1} with 4 cm^{-1} resolution, and the average of 4 readings was taken for FTIR spectra. Magnetization properties were analyzed using vibrating sample magnetometer (VSM) (Cryogenic Limited PPMS). 300 mg nanoparticles were packed inside capsule containers and analyzed in the applied field range of −1 T to 1 T at 298 K. Thermogravimetric analysis was carried out using TA Instruments SDT 650. 10 mg dried sample was heated at a rate of 10°C/min under nitrogen atmosphere. Mass loss of the nanoparticles were plotted as percentage against temperature (100–600°C). Data were analyzed by calculating derivatives of the weight loss. For zeta size analysis, 0.001 g nanoparticles were dispersed in 10 mL of 70% ethanol solution and the experiments were performed using a MALVERN Nano ZS90 to assess surface charge of the nanoparticles.

2.4 | Magnetic field simulations

A magnetic plate placed under a cell culture plate was used to investigate the interaction of nanoparticles with bone cells in the presence of magnetic field. The magnetic field strength inside the individual wells of the cell culture plate was computed using a stationary solver on COMSOL Multiphysics version 5.5. A 3D model of the plate was used with 24 permanent magnets placed under the wells as a 4×6 grid with 18 mm center-to-center distances, leaving an empty well along both directions. The permanent magnets were N35 grade, with 5.06 mm diameter and 1.02 mm thickness.

2.5 | Bone cell interactions

To assess interaction of bone cells with nanoparticles, osteoblasts (hFOB, ATCC-CRL 11372) were cultured using growth media (DMEM supplemented with 10% FBS, 1% penicillin – streptomycin and 1% L – glutamine) under standard cell culture conditions (5% CO_2 at 37°C). Prior to the experiment, nanoparticles were sterilized with 70% (v/v) ethanol and UV-light for 15 min. Osteoblasts were seeded at a density of 20.000 cells/cm^2 and cultured for 24 h. Afterwards, fresh media containing different concentrations of nanoparticles were added onto cells and incubated up to 7 days in vitro. To assess cytotoxicity of the nanoparticles, colorimetric analysis was performed using 3-(4,5-dimethyl-2-thiazolyl)-2,5-diphenyl-2H-tetrazolium bromide (MTT) assay. At the 1st, 3rd, 5th and 7th days of culture, media containing the nanoparticles were aspirated, and cells were rinsed with 1xPBS. 125 μL MTT solution was added into each well and

incubated for 4 h to form formazan crystals. Afterwards, 125 μL isopropanol solution prepared in HCl was added into each well to dissolve the formazan crystals. Optical density was measured using Thermo Scientific Multiskan GO spectrophotometer at 570 nm. MTT data were normalized to no particle control (tissue culture polystyrene) cultured in the absence of magnetic field on day 1, which corresponded to 100% cellular viability. To assess cytotoxicity of the nanoparticles in the presence of external static magnetic field, the same experimental protocol was followed. The only difference was the presence of the magnetic field, where hFOBs were cultured and incubated under constant static magnetic field up to 7 days in vitro. All the cytotoxicity experiments were conducted in triplicate and three samples were run at each time.

2.6 | Antibacterial properties

Prior to the experiments, nanoparticles were sterilized with 70% (v/v) ethanol and UV-light for 15 min. *Staphylococcus aureus* (*S. aureus*, ATCC 25923) and *Pseudomonas aeruginosa* (*P. aeruginosa*, ATCC 27853) were used to assess antibacterial properties of the nanoparticles. Tryptic soy broth (TSB) was used as the culture media. Bacteria were streaked onto tryptic soy agar (TSA) plates to form colonies for 24 h. After 24 h, a single colony was taken from the agar plate and inoculated into tryptic soy broth (TSB) and cultured for 18 h at 200 rpm. The density of the bacteria solution was adjusted with 1xPBS to attain 0.5 in McFarland scale.[27] 100 μL nanoparticle solution and 100 μL bacteria solution were seeded to give 10, 5, 1, 0.5, 0.1, 0.05 and 0.01 g/L nanoparticle concentrations. Nanoparticles were cultured with bacteria for 12, 24, and 48 h at 35°C in the absence and presence of external magnetic field. At the aforementioned time points, cultured bacteria were diluted with 1xPBS up to 6 logs and seeded onto sterile TSA plates. Seeded plates were incubated at 35°C for 24 h and the number of colonies were counted. To calculate inhibition concentration of the synthesized nanoparticles, sigmoidal logistic was used to curve fit, and a dose response function was used to calculate IC50 values for 12 h.

To assess biofilm formation, a similar procedure was followed. Bacteria solutions at 0.5 in McFarland scale were incubated for 24 h to form biofilm. Afterwards, media used to grow the biofilms were discarded and 200 μL TSB solutions containing nanoparticles were added onto the existing biofilms. To understand the interaction of bacteria and nanoparticles, 7 different concentrations of nanoparticle solutions (10, 5, 1, 0.5, 0.1, 0.05 and 0.01 g/L) were seeded onto the biofilms, and incubated for 24 h at 35°C. After 24 h of incubation, TSB solutions were gently discarded. 200 μL 0.1% (w/v) crystal violet (CV) dye was added into each well and incubated for 15 min. At the end of 15 min, each well was delicately rinsed with 1xPBS and air dried. To dissolve the CV dye, biofilms were treated with 99% (v/v) ethanol 15 min. Optical density of the solution was recorded using Thermo Scientific Multiskan GO spectrophotometer at 600 nm. All bacteria experiments were conducted in triplicate and four samples were run at each time.

2.7 | MRI contrast agent performance

To evaluate contrast agent performance of the nanoparticles, the r_1 and r_2 relaxivities of Ch – SPIONs were measured on a 3 T MRI scanner (Siemens Magnetom Trio) using a 32-channel head coil. For these experiments, a dilution series of Ch – SPIONs were prepared in 1.5 mL vials at 7 different iron concentrations of 0.68, 1.37, 2.05, 2.74, 4.10, 5.47, and 6.84 mM. For measuring r_1, a turbo spin echo inversion recovery sequence was utilized, and T_1-weighted imaging was performed at 12 different inversion times (TI) ranging between 24 and 1900 ms with TR/TE = 2000/12 ms. For measuring r_2, a single-echo spin echo sequence was utilized, and T_2-weighted imaging was performed at 12 different echo times (TE) ranging between 10 and 800 ms with TR = 3000 ms. Other imaging parameters that were kept similar for these two sequences were 12 × 12 cm^2 field of view (FOV), and 4 mm slice thickness. The acquisition matrix was 256 × 256 for T_1-weighted imaging and 128 × 102 for T_2-weighted imaging.

The images were analyzed using an in-house MATLAB (Mathworks) script. A fixed size region of interest (ROI) was drawn and placed over the relevant image region of each vial. First, the T_1 value for each sample at each pixel in the ROI was determined using the following inversion recovery equation:

$$S = S_0\left(1 - 2e^{-TI/T_1} + e^{-TR/T_1}\right)$$

Likewise, the T_2 value for each sample at each pixel in the ROI was determined using the following monoexponential decay equation:

$$S = S_0 e^{-TE/T_2}$$

To determine r_1 and r_2, the inverses of T_1 and T_2 as functions of concentration were fitted to linear curves, respectively:

$$\frac{1}{T_1} = \frac{1}{T_{1,0}} + r_1 C$$

$$\frac{1}{T_2} = \frac{1}{T_{2,0}} + r_2 C$$

Here, r_1 and r_2 are the slopes of the linear fits corresponding to the relaxivities, and $T_{1,0}$ and $T_{2,0}$ are the y-intercepts of the fits corresponding to the relaxation times of the medium in the absence of Ch – SPIONs.

2.8 | Statistical analysis

Statistical analyzes were carried out with one-way analysis of variance (ANOVA) in SPSS software using Tukey's post-hoc test. The results were reported as mean ± standard deviation and significance was based on $^*p \le .05$, $^{**}p \le .01$, $^{***}p \le .005$. The coefficients of determination, R^2, for the linear fits for r_1 and r_2 were

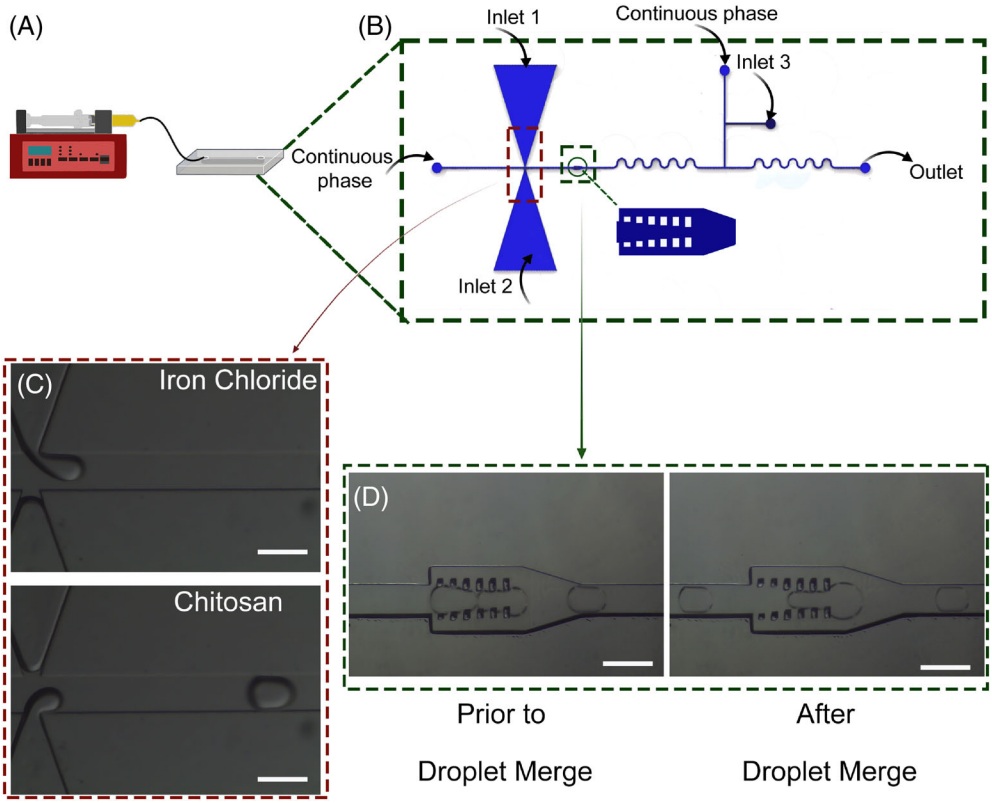

FIGURE 1 Schematic representation of (A) the microfluidic synthesis system and (B) the microfluidic channels used to synthesize SPIONs and Ch – SPIONs. Images of (C) alternating droplet formation and (D) merging of iron and chitosan solution droplets. Scale bars are 50 μm.

computed and an *F* test was used to determine significance level of $^{*}p \leq .05$.

3 | RESULTS AND DISCUSSION

Both SPIONs and Ch – SPIONs were synthesized using a multi-step microfluidic procedure, as shown in Figure 1A,B. For the synthesis of SPIONs, silicon oil was used as a continuous phase which provided formation of alternating droplets, shown in Figure 1C, and iron chloride solutions were supplied from T– junction tapered inlets of the microfluidic channel (inlet 1 and 2). At the region having pillar structures, iron chloride droplets merged with each other, as shown in Figure 1D. Afterwards, the resultant droplet was merged and reacted with the droplet of ammonia solution (introduced from inlet 3). For the synthesis of Ch – SPIONs, silicon oil was again used as the continuous phase, while iron chloride and chitosan solutions were introduced from the T–junction tapered inlet 1 and inlet 2, respectively, into the microchannel. Droplets of iron chloride and chitosan were merged at the pillar array guided channel, where Fe^{2+} and Fe^{3+} ions were captured by the amino groups of chitosan and form chitosan – iron complex.[28] Due to this chelation effect, the amino groups inhibited the spread of iron ions and controlled the growth of magnetic crystals.[28] Subsequently, a droplet of ammonia solution was merged with chitosan – iron complex and led to the formation of the SPIONs. Ammonia improved homogeneity and prevented the formation of agglomerates during crystal growth. As both particles formed, color change was observed in the droplets; SPIONs turned into a black precipitate and Ch – SPIONs turned into an orange precipitate. This multi-step procedure in a microreactor allowed control of reaction kinetics and physicochemical properties of the nanoparticles during their synthesis.[29,30] Video of the microfluidic channels and droplets captured during particle synthesis were provided in the Figure S1.

SEM and TEM investigations of the particles confirmed that both SPIONs and Ch – SPIONs had a particle size in the nanometer scale (Figure 2A–D).

Energy dispersive x-ray spectroscopy (EDAX) analysis revealed that Ch – SPIONs have higher carbon percentage (34.6% wt.) compared to SPIONs (2.5% wt.) due to the presence of hydrocarbon-based chitosan (Figure S2). Concurrently, concentration of iron decreased from 77.4% wt. for the SPIONs to 39.9% wt. for the Ch – SPIONs. TEM investigations revealed that both nanoparticles had a spherical morphology with a uniform size distribution (Figure 2C,D). The average size of the SPIONs was 6.8 ± 0.6 nm, whereas composite formation with chitosan increased the particle size to 8.8 ± 1.2 nm, as shown in Table 1. The rings observed for the electron diffraction pattern indicated polycrystalline nature of SPIONs in Figure 2E,F.

XRD spectra of the nanoparticles further confirmed the crystalline nature of SPIONs and Ch – SPIONs (Figure 3A).[31] The characteristic peaks of SPIONs were observed for both nanoparticles at 2θ 30.25°(220), 35.58°(311), 43.17°(400), 53.46°(422), 57.13°(511), and 62.72°(440), which was the standard pattern for crystalline magnetite having spinel structure (JCPDS – 19 – 0629).[31] This result was in-line with the selected area diffraction pattern of SPIONs, as shown in Figure 2E,F. Although relative intensities of the characteristic

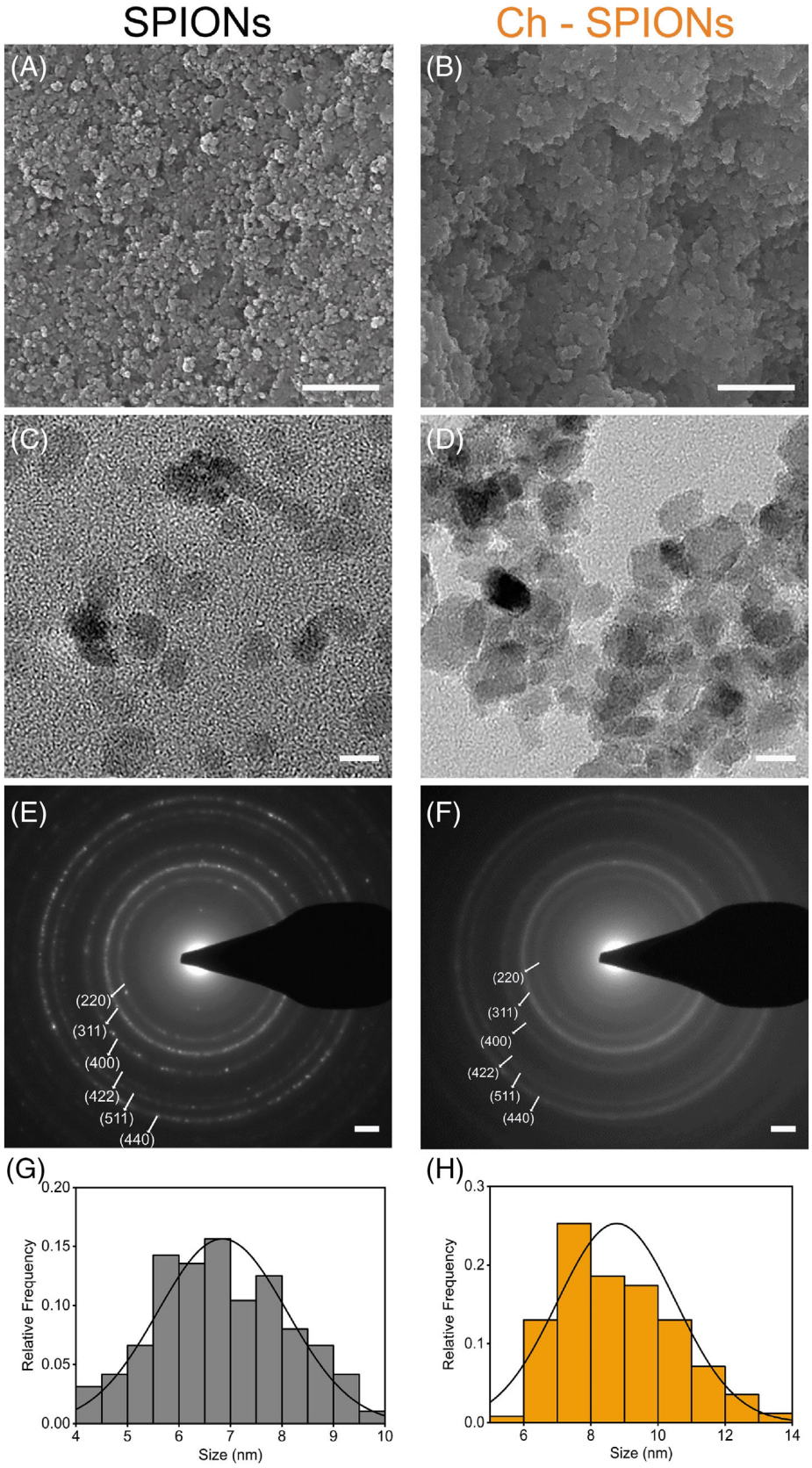

FIGURE 2 (A–B) SEM images of (A) SPIONs and (B) Ch – SPIONs (scale bars are 1 μm). (C–D) TEM images of (C) SPIONs and (D) Ch – SPIONs (scale bars are 10 nm). (E–F) Diffraction patterns of (E) SPIONs and (F) Ch – SPIONs (scale bars are 1 1/nm). (G–H) Particle size distributions for (G) SPIONs and (H) Ch – SPIONs.

crystalline peaks decreased for Ch – SPIONs, composite nanoparticle formation using chitosan during particle synthesis did not lead to any peak shift or phase change.

Specific molecular vibrations of the chemical bonds were shown in the FTIR spectra of the nanoparticles (Figure 3B). Both SPIONs and Ch – SPIONs had a peak at around 572 cm^{-1}, which was the Fe—O

TABLE 1 Size and zeta potential values of SPIONs and Ch – SPIONs.

	SPIONs	Ch – SPIONs
Size (nm)	6.8 ± 0.6	8.8 ± 1.2
Zeta Potential (mV)	−19.8 ± 1.1	23.7 ± 0.5

stretching vibration of tetrahedral sites of spinel structure.[32] This peak further confirmed the presence of Fe_3O_4 in Ch – SPIONs. The peak at 872 cm^{-1} belonged to Fe—O stretching vibration, which was only observed for the SPIONs. The peaks at 1061, 1153, 1319, 1416 and 1456 cm^{-1} were stretching vibrations of C—O, C—O—C bridge, C—N for amide III, C—N, and C—H groups in chitosan,[28,33,34] respectively, which were only present for Ch – SPIONs, and thus, confirmed the presence of chitosan for Ch – SPIONs. The peaks at 3429 and 1627 cm^{-1} were stretching and bending of OH groups of water, which was adsorbed by the nanoparticles, respectively.[35]

Thermal stability of SPIONs and Ch – SPIONs were investigated up to 600°C, as shown in Figure 3C. When SPIONs were heated from 25 to 600°C, physically and chemically water removed from the particles at this temperature range. The total weight loss for SPIONs was around 13%. The obtained weight loss curve was in-line with the findings in literature.[28] Based on the TGA curves, Ch – SPIONs also had three decomposition stages; the first one occurred between 25 and 156°C, the second one occurred between 156 and 385°C and the third one occurred above 385°C.[36] In the first stage, mass loss of Ch – SPIONs was due to the removal of adsorbed water, and it was approximately 7.2 wt.%. In the second stage, decomposition of chitosan took place and there was a total mass loss of 26.1 wt.%, and it could mostly be attributed to the deacetylation of chitosan and cleavage of glycoside bonds via dehydration and deamination.[36,37] Weight loss after 385°C could be explained with thermal devastation of pyranose ring, which resulted in the production of formic acid and butyric acid,[37] and total weight loss of Ch – SPIONs was nearly 36.9%. Since Ch – SPIONs had a higher percent weight loss compared to SPIONs, TGA results further confirmed the presence chitosan for the Ch – SPIONs.

Magnetic properties of both nanoparticles were determined using VSM (Figure 3D). The saturation magnetization values for SPIONs and Ch – SPIONs were measured to be 54.8 and 32.0 emu/g, respectively. The M – B curves showed that both nanoparticles exhibited superparamagnetic characteristics with zero coercivity and remanence; however, Ch – SPIONs had lower magnetization than pure SPIONs due to the chitosan layer surrounding the nanoparticles.

The suspension of SPIONs in water was unstable (Figure S3) and it agglomerated in 30 min due to the presence of highly attractive Van Der Waals and magnetic dipolar forces between the nanoparticles.[2] Composite nanoparticle formation of SPIONs with chitosan enhanced their stability and Ch – SPIONs dispersed better in aqueous environment. Zeta potential values of the nanoparticles were measured to be −19.8 ± 1.1 and 23.7 ± 0.5 mV for SPIONs and Ch – SPIONs, respectively (Table 1). Since SPIONs had a lower absolute surface charge, they tended to agglomerate in aqueous medium at neutral pH. Very small particle size and high surface area to volume ratio of SPIONs could have also contributed to the agglomeration tendency of these nanoparticles.[38] However, composite nanoparticle formation to synthesize Ch – SPIONs provided additional surface charge to SPIONs, which provided higher electrostatic repulsion, along with steric effects inside aqueous medium.[39,40] Dispersibility of the nanoparticles highly affected their MRI contrast agent performance. Example T_1- and T_2-weighted MRI images (Figure 4A), and MRI contrast performance evaluations (Figure 4B,C) for Ch – SPIONs were investigated. According to the linear fits in Figure 4B,C, the measured relaxivities at 3 T for Ch – SPIONs were $r_1 = 0.484\ mM^{-1}\ s^{-1}$ and $r_2 = 7.764\ mM^{-1}\ s^{-1}$.

Similar experiments were also performed for SPIONs. However, due to their colloidal instability in water, SPIONs immediately agglomerated to the bottom of the vials, rendering the MRI relaxivity measurements impractical. In contrast, Ch – SPIONs displayed good colloidal stability at various concentrations, as reflected by the small error bars and excellent linear fits in Figure 4B,C. The coefficients of determination for r_1 and r_2 were equal to $R^2 = 0.997$ ($^*p < .05$) and $R^2 = 0.999$ ($^*p < .05$), respectively. These results showed that Ch – SPIONs had relatively high r_2 relaxivities comparable to those in the literature,[5,41,42] and a moderate-to-low r_1 relaxivity. Contrast agents with high r_2 relaxivities produce negative contrast (i.e., locally reduced signal) in MRI images due to their capability to shorten transverse (T_2) relaxation of the surrounding tissue.[43] On the other hand, contrast agents with high r_1 relaxivities produce positive contrast (i.e., locally increased signal) in MRI images by shortening the longitudinal (T_1) relaxation.[43] By locally reducing the MRI signal, Ch-SPIONs can provide improved visibility and reliable, accurate diagnosis and monitoring of infection and inflammation.

Aside from improved MRI visibility, SPIONs would also allow for magnetic targeting of the nanoparticles to desired tissues. To test the biological performance of microfluidically synthesized SPIONs and Ch – SPIONs under external magnetic targeting, we designed a magnetic plate where neodymium magnets were placed to every other well, and this magnetic plate was secured beneath a 96-well tissue cell culture plate used for the biological experiments[44] (Figure 5A). Prior to the experiments, magnetic field strengths in the x, y and z planes were computed in COMSOL, as displayed in Figure 5B, as the highest field strength was shown in red color and the lowest field strength was shown in blue color. The spacing of the magnets by leaving one empty well in between ensured identical magnetic field conditions within each of the 24 wells with a mean strength of 0.4 T at the tissue culture plate surface.

The colorimetric MTT assay was used to assess cellular viability of hFOBs cultured with SPIONs and Ch – SPIONs at 5 different nanoparticle concentrations (10, 5, 1, 0.5, 0.1 g/L) up to 7 days in vitro in the presence and absence of external static magnetic field (Figure 5 and Figure S4). The experiments conducted in the absence of external static magnetic field (Figure 5C–F) showed that hFOBs successfully proliferated up to 7 days upon the interaction with both SPIONs and Ch – SPIONs. Interestingly, SPIONs promoted higher hFOB viability than Ch – SPIONs up to 7 days (Figure 5C–F) independent of the

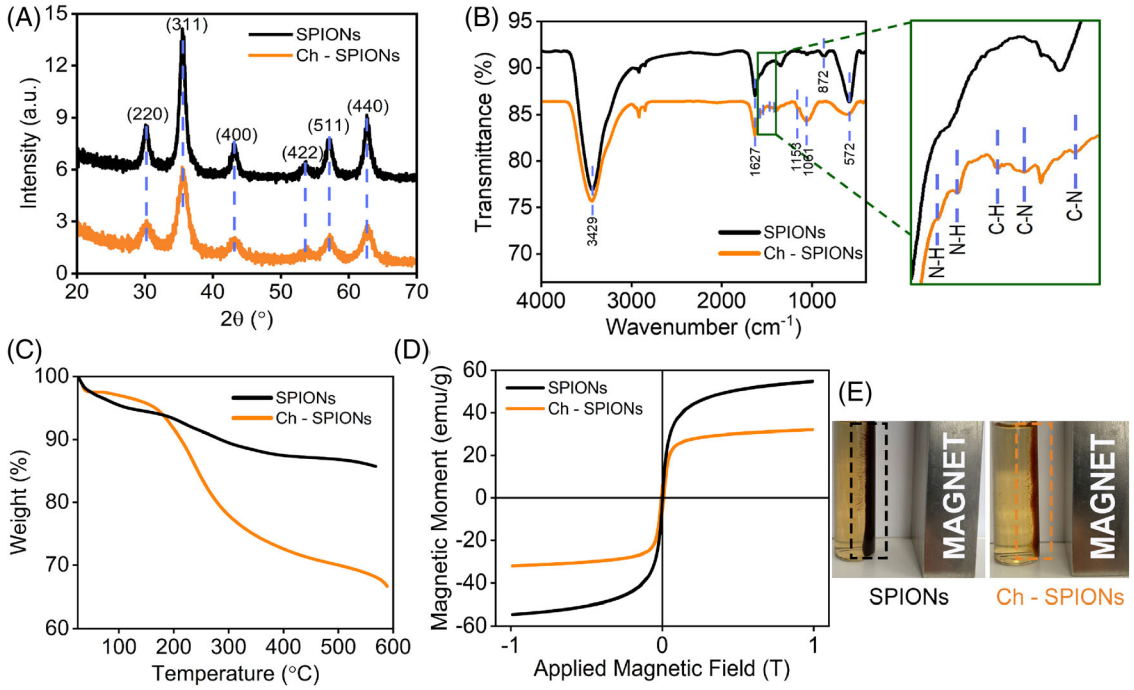

FIGURE 3 (A) XRD (n = 3) and (B) FTIR spectra of the nanoparticles (n = 4). (C) Thermogravimetric analysis and (D) magnetic properties of the nanoparticles. (E) Photograph showing the magnetic response of SPIONs and Ch – SPIONs towards a Nd – Fe – B magnet.

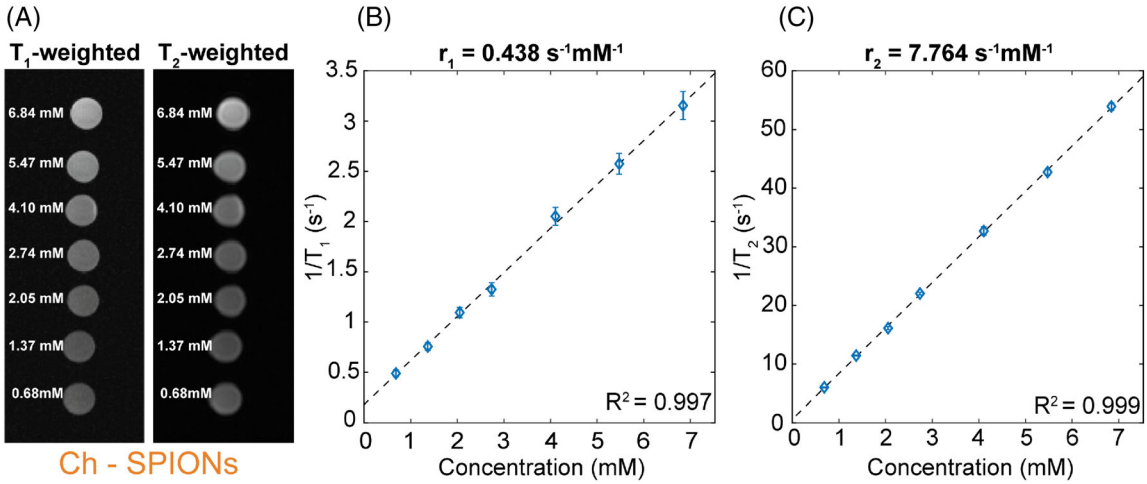

FIGURE 4 (A) Example T_1-weighted and T_2-weighted MRI images at 3 T for Ch – SPIONs. Measured relaxivities were (B) $r_1 = 0.484\ mM^{-1}\ s^{-1}$ and (C) $r_2 = 7.764\ mM^{-1}\ s^{-1}$ for Ch – SPIONs at 3 T. Graphics display changes in the relaxation rates (i.e., inverses of T_1 and T_2 relaxation times) for 0.68, 1.37, 2.05, 2.74, 4.10, 5.47 and 6.84 mM iron concentrations. Relaxation rates are plotted as mean ± SD over all pixels in ROIs, and the dashed lines show linear fits with slope corresponding to r_1 or r_2.

nanoparticle concentration. For example, for the lowest particle concentration of 0.1 g/L, the viability of hFOBs was 79, 58, 42 and 47% lower for Ch – SPIONs compared to SPIONs at the 1st, 3rd, 5th and 7th days of culture, respectively, in the absence of magnetic field (Figure 5C–F). For the highest particle concentration (10 g/L), the viability of hFOBs was 74%, 56%, and 55% lower for Ch – SPIONs compared to SPIONs at the 1st, 5th, and 7th days, respectively, in the absence of magnetic field (Figure 5C–F). For both nanoparticles, the highest nanoparticle concentration exhibited the lowest hFOB viability. In fact, decreasing the concentration of the nanoparticles increased cellular viability in a dose-dependent manner. This trend was evident when maximum and minimum nanoparticle concentrations were compared. For instance, in the absence of magnetic field, hFOB viability was 83%, 79%, 58%, and 50% lower for SPIONs having 10 g/L concentration compared to SPIONs having 0.1 g/L concentration at 1st, 3rd, 5th, and 7th days, respectively (Figure S4A).

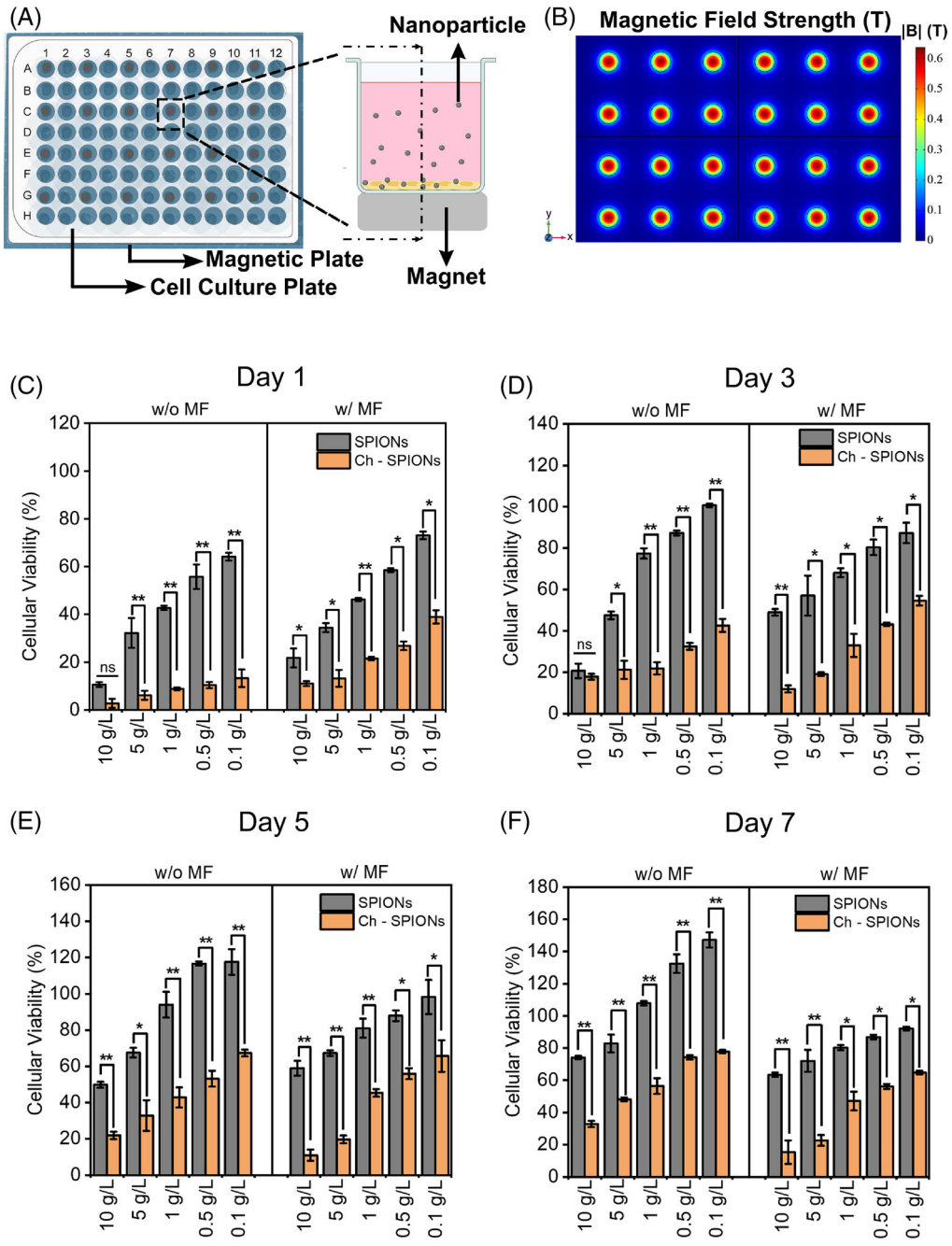

FIGURE 5 (A) Schematic representation of the magnetic plate (light blue), the cell culture plate, and the positioning of an individual magnet once magnetic plate was secured beneath the cell culture plate. (B) Two-dimensional magnetic field strength map at the cell culture plate surface. MTT assay results of human fetal osteoblast (hFOB) viability in the absence (w/o) and presence (w/) of external static magnetic field (MF) cultured with 10, 5, 1, 0.5, 0.1 g/L nanoparticles at (C) 1, (D) 3, (E) 5, and (F) 7 days of culture in vitro. Values are mean±SD (n = 3), $^{*}p < .05$, $^{**}p < .01$, ns: no significant difference.

For Ch – SPIONs, the viability of hFOBs was 79%, 58%, 68%, and 58% lower for 10 g/L Ch – SPIONs concentration compared to 0.1 g/L concentration at the 1st, 3rd, 5th, and 7th days, respectively (Figure S4C).

Similar trends were also observed when hFOB – nanoparticle interactions occurred in the presence of external static magnetic field (Figure 5C–F, and Figure S4). Similar to the no static magnetic field results, SPIONs promoted higher hFOB viability than Ch – SPIONs up to 7 days in vitro at all nanoparticle concentrations (Figure 5). For instance, in the presence of external magnetic field, the viability of hFOBs was 47%, 37%, 33%, and 30% lower for Ch – SPIONs compared to SPIONs for the lowest particle concentration of 0.1 g/L at the 1st, 3rd, 5th, and 7th days, respectively (Figure 5C–F). Furthermore, the highest particle concentration (10 g/L) decreased the

viability of hFOBs by 49%, 76%, 81%, and 76% for Ch – SPIONs compared to SPIONs at the 1st, 3rd, 5th, and 7th days of culture, respectively (Figure 5C–F). Furthermore, hFOBs showed dose-dependent decrease in their viability for both SPIONs and Ch – SPIONs under external static magnetic field, and the differences between hFOB viability was the most apparent when maximum and minimum nanoparticle concentrations were compared. hFOB viability was 70%, 44%, 40%, and 31% lower for SPIONs having 10 g/L concentration compared to the ones having 0.1 g/L concentration at the 1st, 3rd, 5th, and 7th days of culture, respectively (Figure S4B). For the case of Ch – SPIONs, the viability of hFOBs was 72%, 78%, 83%, and 76% lower for 10 g/L compared to 0.1 g/L nanoparticle concentration at the 1st, 3rd, 5th, and 7th days of culture, respectively (Figure S4D). It was critical to note that the influence of external magnetic field on hFOB viability depended both on the type and their concentration of the nanoparticles. Under the external magnetic field, hFOBs proliferated and their viability increased with time up to 7 days in vitro for all SPIONs concentration. However, hFOB proliferation was compromised at high Ch – SPIONs concentrations (5 and 10 g/L), where cellular viability did not significantly increase with time. On the other hand, lower Ch – SPIONs concentrations (1, 0.5, 0.1 g/L) still promoted viability of hFOBs, which suggested Ch – SPIONs concentrations less than 1 g/L to support hFOB proliferation. Figure S4E–H showed hFOB morphologies at the 3rd day cultured with 0.5 g/L concentration of nanoparticles in the presence and absence of external static magnetic field. hFOBs cultured with both SPIONs and Ch – SPIONs were healthy and exhibited a well-spread cellular morphology. Moreover, hFOBs were not observed to change their cellular morphology under the magnetic field.

Since the biocompatibility of chitosan depended on its degree of acetylation and molecular weight, where 7–23 kDa molecular weight and 7%–34% degree of acetylation favored biocompatibility,[45] it was possible that high molecular weight and high degree of acetylation of chitosan might have contributed to the decreased cellular viability upon composite nanoparticle formation with SPIONs.[45] It could be speculated that hFOBs' cellular membrane showed higher permeability to Ch – SPIONs due to the positively charged chitosan layer,[46] which led to compromised hFOB viability. Having this said, magnetic field also affected hFOB viability in the presence of nanoparticles. Although 0.4 T static magnetic field was not found to effect hFOB viability, which was in-line with literature,[47,48] the effect of magnetic field on hFOB viability was different depending on if SPIONs or Ch – SPIONs were used for the experiments. While high nanoparticle concentrations (5 and 10 g/L) maximized the difference in the cellular viability of hFOBs for SPIONs and Ch – SPIONs, as the nanoparticle concentration decreased (1, 0.5, 0.1 g/L), the difference between the cellular viability of hFOBs for SPIONs and Ch – SPIONs diminished. It was possible that Ch – SPIONs, which were shown to limit hFOB viability more than SPIONs, were internalized into the cells more effectively under external static magnetic field, and thus, they further decreased hFOB viability at high Ch – SPIONs concentrations. On the other hand, under the magnetic field, as hFOBs cultured with SPIONs reached confluency, their proliferation slowed down, which led to diminished differences in the hFOB viability between SPION and Ch – SPION treated groups. Having this said, the external static magnetic field was shown to increase viability of hFOBs at high SPION concentrations compared to non-magnetically stimulated hFOBs, while the effect of external static magnetic field was not evident at low SPION concentrations. However, the reason for increased hFOB viability at high SPION concentrations in the presence of the external static magnetic field was not clear, moderate static magnetic field was shown to increase the percentage of cells in their growth phase, while decreasing the percentage of cells in their DNA replication phase.[49] Cumulatively, these results showed that hFOBs were continuously proliferating up to 7 days in vitro upon the culture with 1, 0.5 and 0.1 g/L Ch – SPIONs independent of the presence or absence of external static magnetic field.

To assess antibacterial performance of the nanoparticles, SPIONs and Ch – SPIONs were cultured with gram-positive *S. aureus* and gram-negative *P. aeruginosa* up to 48 h in vitro in the absence and the presence of magnetic field. The results showed that both SPIONs and Ch – SPIONs exhibited antibacterial activity compared to no particle tissue culture polystyrene (TCPS) controls (Figures 6, and 7; Figures S5 and S6). Agar plates of *S. aureus* and *P. aeruginosa* colonies cultured with different concentrations of Ch – SPIONs were also shown in Figures 6 and 7. Similar to the cytotoxicity experiments, a concentration dependent decrease in the number of colonies was observed for both bacteria strains upon culturing with SPIONs and Ch – SPIONs (Figures 6 and 7; Figures S5 and S6). Although the results showed that all concentrations of SPIONs and Ch – SPIONs (10, 5, 1, 0.5, 0.1, 0.05, 0.01 g/L) led to a significant reduction in the number of colonies against both *S. aureus* and *P. aeruginosa* after 12, 24, and 48 h, Ch – SPIONs showed better antibacterial properties compared to SPIONs against both bacteria strains and this trend was evident at higher nanoparticle concentrations (Figure 6). For example, for the highest nanoparticle concentration of 10 g/L, Ch – SPIONs decreased number of *S. aureus* colonies by 53%, 80%, and 73% more compared to SPIONs at 12, 24, and 48 h of culture, respectively (Figure 6A–C). The trend for larger decrease in bacteria colonies for Ch – SPIONs compared to SPIONs was also observed for *P. aeruginosa*. For 10 g/L nanoparticle concentration, the number of *P. aeruginosa* colonies was 56%, 23%, and 13% lower for Ch – SPIONs compared to SPIONs at 12, 24, and 48 h, respectively (Figure 6D–F). Moreover, in the absence of magnetic field, the number of *S. aureus* colonies decreased by 89% and 52% upon culturing with SPIONs having 10 g/L concentration compared to the ones cultured with 0.01 g/L SPIONs at 12 and 48 h, respectively (Figure S5A). Furthermore, the number of *S. aureus* colonies was 94% and 85% lower when they interacted with 10 g/L compared to 0.01 g/L Ch – SPIONs at 12 and 48 h, respectively (Figure S5C). For the case of *P. aeruginosa*, the number of colonies was 69% and 52% lower when they interacted with 10 g/L compared to 0.01 g/L SPIONs at 12 and 48 h, respectively (Figure S5B). Moreover, the number of *P. aeruginosa* colonies was 84% and 58% lower they interacted with 10 g/L compared to 0.01 g/L Ch – SPIONs at 12 and 48 h, respectively (Figure S5D). The

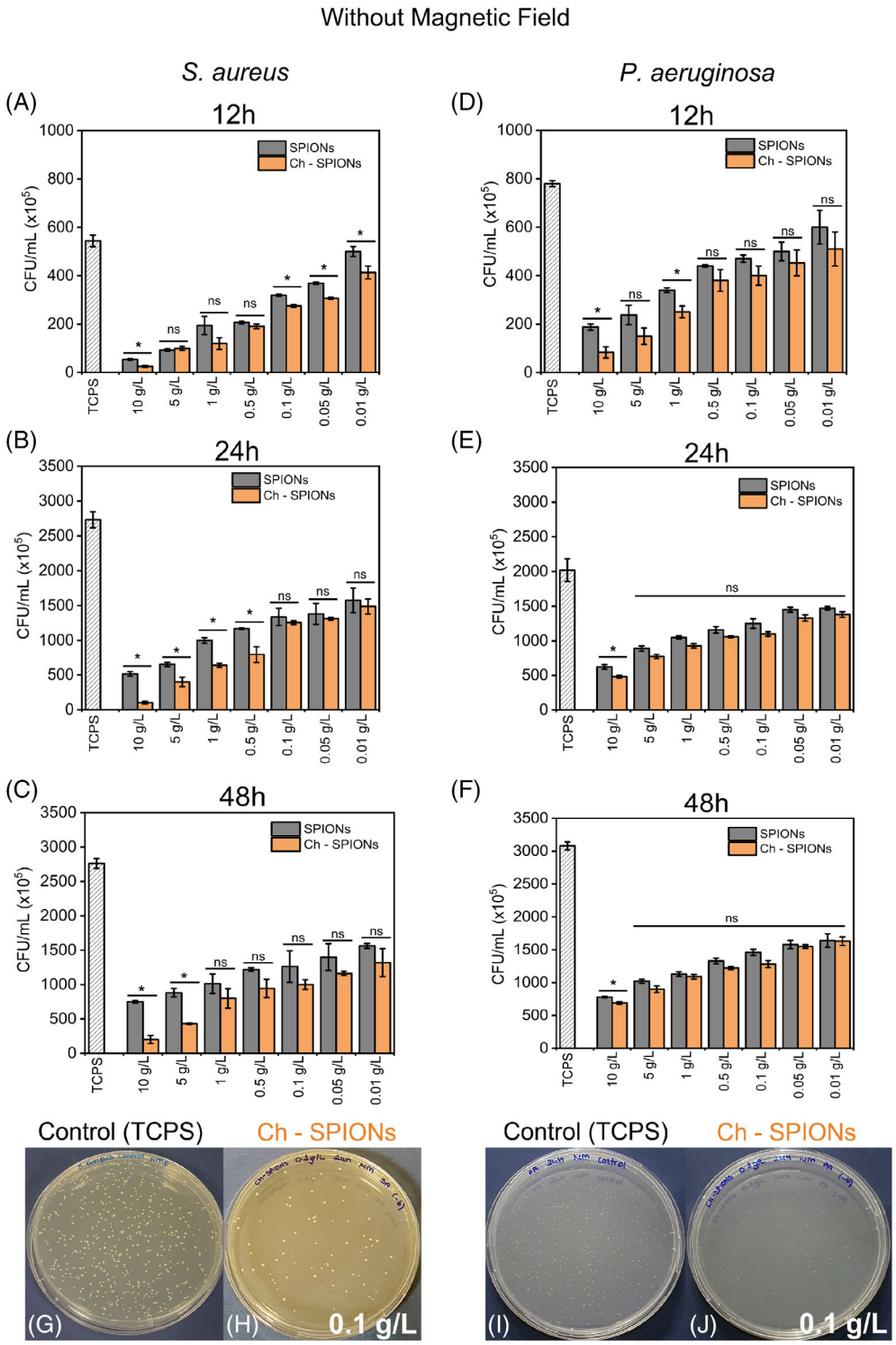

FIGURE 6 The number of (A), (B) and (C) *S. aureus* and (D), (E), and (F) *P. aeruginosa* colonies cultured with 10, 5, 1, 0.5, 0.1, 0.05, 0.01 g/L SPIONs and Ch – SPIONs for (A) and (D) 12 h, (B) and (E) 24 h, (C) and (F) 48 h in vitro in the absence of magnetic field. Values are mean ± SD (n = 3), *$p < .05$, ns: no significant difference. Photographs of (G–H) *S. aureus*, and (I–J) *P. aeruginosa* colonies at −6 dilution (G) and (I) for TCPS controls (no particles), (H) and (J) upon culturing with 0.1 g/L Ch – SPIONs.

higher antibacterial efficacy of Ch – SPIONs compared to SPIONs was also evident in their IC50 values (Table 2). The IC50 values for SPIONs and Ch – SPIONs against *S. aureus* were 0.13 ± 0.04 and 0.08 ± 0.01 g/L, respectively. For *P. aeruginosa*, IC50 values for SPIONs and Ch – SPIONs were 0.75 ± 0.04 and 0.45 ± 0.01 g/L, respectively. Higher IC50 values for both nanoparticles against *S. aureus* would indicate that these nanoparticles were more effective against *S. aureus* than *P. aeruginosa*.

Since Ch – SPIONs concentrations lower than 1 g/L promoted osteoblast viability and proliferation both in the presence and absence of external static magnetic field, and at the same time exhibited antibacterial properties against *S. aureus* than *P. aeruginosa*, 1 and 0.1 g/L Ch – SPIONs were tested for their antibacterial efficacy in the presence of magnetic field up to 48 h (Figure 7 and Figure S6). Both nanoparticle concentrations showed reduction in the number of *S. aureus* and *P. aeruginosa* colonies at the investigated time points. For

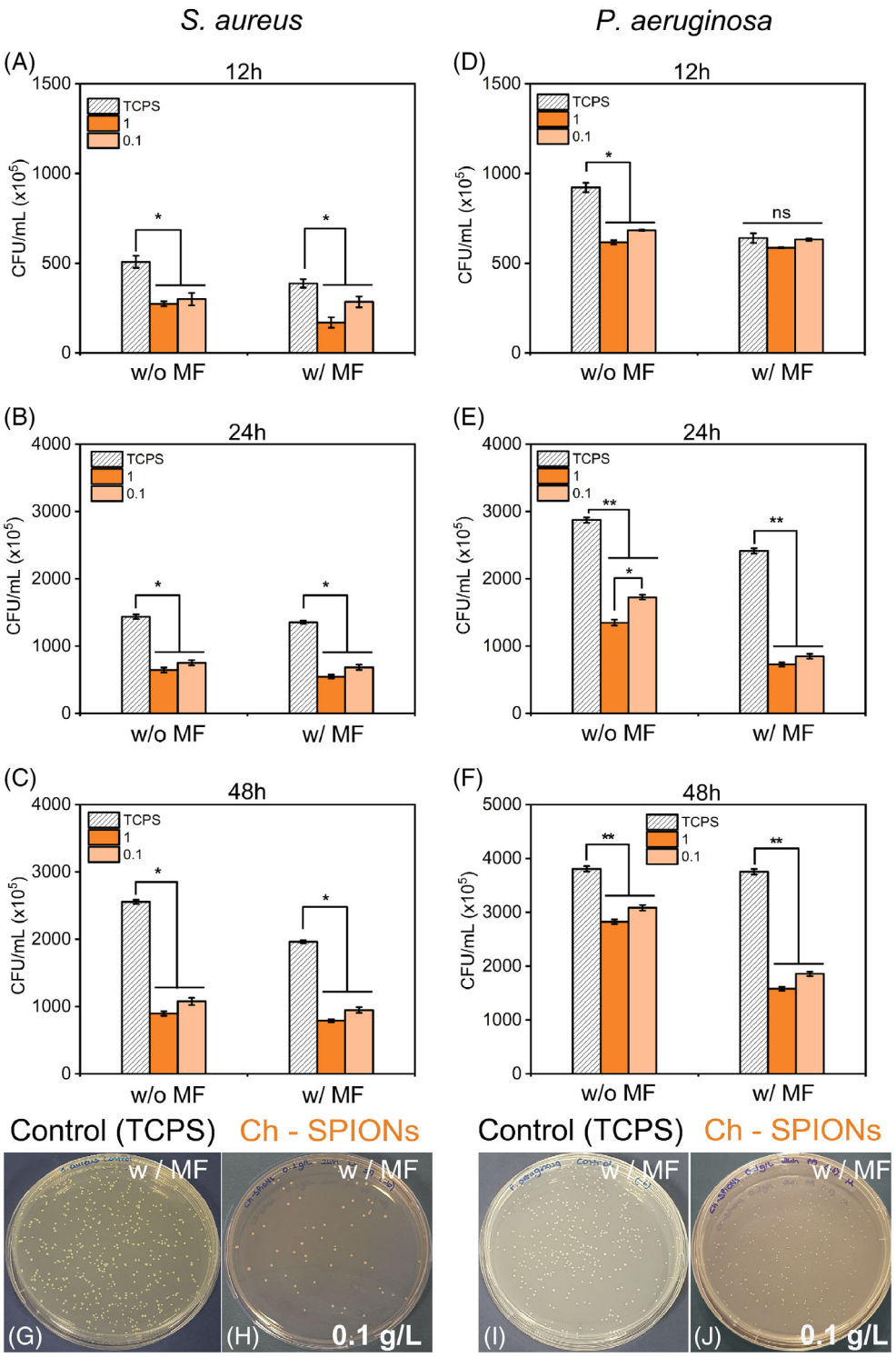

FIGURE 7 Number of (A–C) *S. aureus*, and (D–F) *P. aeruginosa* colonies cultured with Ch – SPIONs at 1, 0.1 g/L nanoparticle concentrations up to 48 h in the presence of magnetic field. Values are mean ± SD (n = 3), *p < .05, **p < .01, ns: no significant difference. Photographs of (G–H) *S. aureus*, and (I–J) *P. aeruginosa* colonies at −6 dilution for (G) and (I) TCPS controls (no particles), (H) and (J) upon culturing with 0.1 g/L Ch – SPIONs at 24 h in the presence of magnetic field.

TABLE 2 IC50 values of SPIONs and Ch – SPIONs against *S. aureus* and *P. aeruginosa*.

	SPIONs	Ch – SPIONs
S. aureus (g/L)	0.13 ± 0.04	0.75 ± 0.04
P. aeruginosa (g/L)	0.08 ± 0.01	0.45 ± 0.01

instance, when Ch – SPIONs interacted with *S. aureus* at 1 g/L concentration for 48 h in the presence of magnetic field, the number of *S. aureus* colonies was 59% lower compared to TCPS controls. For 0.1 g/L concentration, Ch – SPIONs decreased the number of *S. aureus* colonies by 52% compared to TCPS at 48 h of culture. Similar trends were observed for the *P. aeruginosa* strain. In the presence

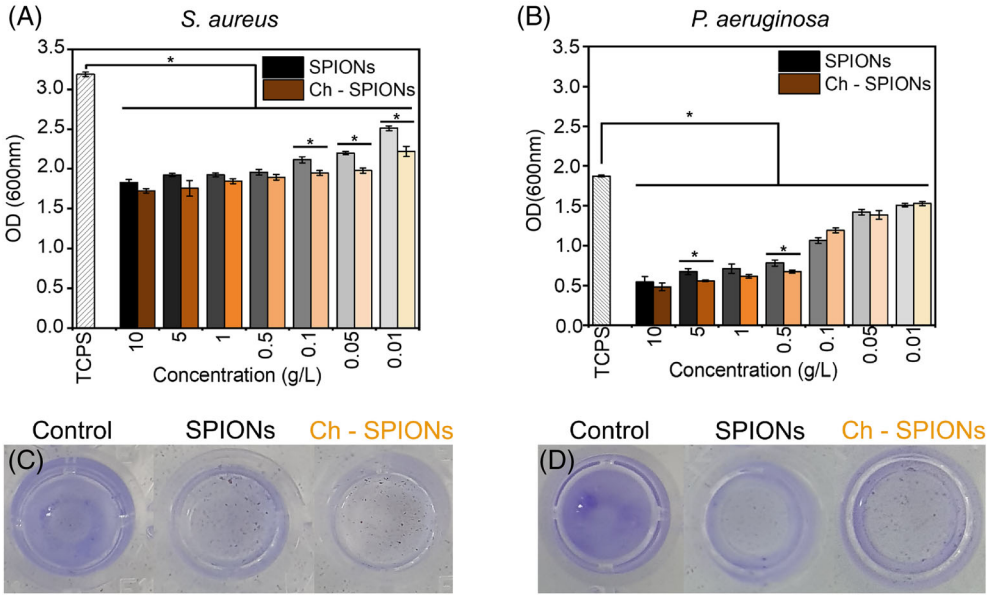

FIGURE 8 (A) *S. aureus* and (B) *P. aeruginosa* biofilm growth cultured with 10, 5, 1, 0.5, 0.1, 0.05, 0.01 g/L SPIONs and Ch – SPIONs up to 24 h. Crystal violet staining of (C) *S. aureus* and (D) *P. aeruginosa* biofilms cultured with 0.1 g/L SPIONs and Ch – SPIONs at 24 h of culture (*$p < .05$).

of magnetic field, 1 g/L concentration of Ch – SPIONs decreased the number of *P. aeruginosa* colonies by 56% compared to TCPS at 48 h of culture. For 0.1 g/L concentration, the number *P. aeruginosa* colonies were 51% lower compared to TCPS at 48 h, respectively. Application of a magnetic field reduces bacterial growth, regardless of its strength and uniformity. To further investigate this effect in our study, nanoparticles were incubated with both bacteria strains in the absence and presence of a magnetic field. The results showed that the number of *P. aeruginosa* colonies for the control samples incubated in the presence of magnetic field was 31% and 16% lower compared to the control samples incubated in the absence of a magnetic field at 12 and 24 h, respectively. Similarly, the number of *S. aureus* colonies for the control samples incubated in the presence of a magnetic field was 24% and 23% lower compared to the control samples incubated in the absence of magnetic field at 12 and 48 h, respectively. When bacteria were incubated with Ch-SPIONs, bacterial growth was further reduced for both strains. For instance, the number of *P. aeruginosa* colonies was 44% and 40% lower at 1 and 0.1 g/L concentrations, respectively, in the presence of magnetic field compared to their counterparts cultured in the absence of magnetic field at 48 h. It is interesting to note that for *S. aureus*, magnetic field did not further enhance the antibacterial activity of Ch – SPIONs. On the other hand, for *P. aeruginosa* the magnetic field improved the antibacterial activity Ch – SPIONs. Although the reasons for this trend are not clear, the differences in the internalization of the nanoparticles across the bacterial membranes might have contributed to these findings. Further research is required to better understand this trend.

The effect of SPIONs and Ch – SPIONs on eliminating existing biofilms were tested with different nanoparticle concentrations (10, 5, 1, 0.5, 0.1, 0.05, 0.01 g/L) using crystal violet (CV) staining, and the results were shown in Figure 8. Similar to the colony growth results, there was a concentration dependent antibacterial response of both nanoparticles towards *S. aureus* and *P. aeruginosa*. Ch – SPIONs were observed to limit biofilm growth more than SPIONs for both *S. aureus* and *P. aeruginosa* (Figure 8). At the highest nanoparticle concentration of 10 g/L, Ch – SPIONs and SPIONs decreased *S. aureus* biofilm growth by 46% and 43%, respectively, at 24 h of culture (Figure 8A). As the concentration of the nanoparticles decreased, the inhibitory effect of Ch – SPIONs compared to SPIONs became evident. For the lowest nanoparticle concentration of 0.01 g/L, Ch – SPIONs and SPIONs decreased *S. aureus* biofilm growth by 30% and 21%, respectively (Figure 8A). A similar trend of reduced biofilm growth was also observed when the nanoparticles interacted with *P. aeruginosa*. For the highest nanoparticle concentration of 10 g/L, Ch – SPIONs and SPIONs decreased *P. aeruginosa* biofilm growth by 74% and 71%, respectively, at 24 h of culture (Figure 8B). At 0.01 g/L concentration, Ch – SPIONs and SPIONs decreased *P. aeruginosa* biofilm growth by 18% and 19%, respectively. Crystal violet staining of *S. aureus* and *P. aeruginosa* biofilms cultured with 0.5 g/L SPIONs and Ch – SPIONs at 24 h of culture was displayed in Figure 8C,D.

The antibacterial effect of nanoparticles towards these bacteria strains could be explained with surface charge-based electrostatic interactions between the nanoparticles and the bacteria. These electrostatic interactions were reported to increase production of reactive oxygen species (ROS) for both SPIONs and Ch – SPIONs,[50] which could explain the concentration dependent antibacterial activity of both nanoparticles observed in this study. Since *S. aureus* and *P. aeruginosa* are negatively charged, the positively charged Ch – SPIONs were electrostatically attracted by these bacteria strains,[51] and generated radicals,[9] which eventually led to destruction of the bacteria.[9] In fact, the positively charged Ch – SPIONs was shown to generate higher amounts of radicals than SPIONs.[9] It could be speculated that high concentrations of both nanoparticles, as well as stronger nanoparticle – bacteria interactions for Ch – SPIONs favored higher antibacterial activity. Yet, at lower concentrations (less than 1 g/L), there was no significant difference between SPIONs and Ch – SPIONs. Considering the antibacterial nature of chitosan, its concentration was critical in the antibacterial performance of the

composite nanoparticles. Perhaps, as the concentration of Ch – SPION nanoparticles increased, so did the concentration of antibacterial chitosan available to fight bacteria. This also explained why the difference between SPIONs and Ch – SPIONs increased in a concentration dependent manner. It was interesting to note that both nanoparticles were more effective in limiting existing biofilm growth of *P. aeruginosa* compared to *S. aureus*. This was a counterintuitive finding since outer membrane of gram-negative bacteria typically posed an additional barrier to molecular entry into the cells.[52] In fact, the IC50 values of the nanoparticles against bacteria colonies showed an opposite trend and exhibited lower IC50 values for both nanoparticles against *S. aureus* colonies than *P. aeruginosa* colonies (Table 2).

Apparently, the formation of biofilm was altering the antibacterial efficacy of the nanoparticles. The inhibitory effect of nanoparticles on the existing biofilms of *P. aeruginosa* and *S. aureus* could be correlated with colloidal stability of the nanoparticles. As stated previously, SPIONs quickly agglomerated and formed large particles, however, Ch – SPIONs exhibited more stable characteristics in aqueous conditions (Figure S3). It was possible that Ch – SPIONs were able to penetrate water channels of the biofilm more effectively, while the increased particle size of SPIONs limited their penetration into the biofilm. Once Ch – SPIONs penetrated into the biofilms, the opposite charges between chitosan and bacteria cell wall could have further enhanced the antibacterial effect of Ch – SPIONs.[53]

Herein, SPIONs were synthesized and combined with chitosan to fabricate SPION – Chitosan composite nanoparticles using a novel microfluidics method. Using chitosan solution prior to nucleation of SPIONs limited spreading of the iron ions which controlled the size of magnetite crystal and provided better stability during nanoparticle synthesis.[28] The microfluidic approach provided control over the particle size and size distribution, while the process was low cost, reproducible, and scalable. In literature, batch synthesis with co-precipitation was the most widely used method to synthesize SPIONs, however, it is difficult to control the physicochemical properties of the nanoparticles. For instance, when Ch – SPIONs were synthesized with the batch technique, the obtained particles were 21 nm in size, while our microfluidic technique generated 8.8 ± 1.2 nm sized particles.[54] Besides, microfluidic approach allowed processing of the nanoparticles within the same device, where SPIONs were in-situ coated with antibacterial chitosan inside the microfluidics device without any need for post processing. The microfluidically synthesized Ch – SPIONs were shown to maintain their functionality; they exhibited superparamagnetic properties with a magnetization value of 32.0 emu/g and showed antibacterial activity against *S. aureus* and *P. aeruginosa*. They exhibited antibacterial activity against planktonic phase *S. aureus* and *P. aeruginosa* at all investigated nanoparticle concentrations. Furthermore, these particles were shown to be effective against *S. aureus* and *P. aeruginosa* biofilms at concentrations as low as 0.01 g/L. Importantly, for Ch – SPIONs concentrations less than 1 g/L, it was shown that they reduce *S. aureus* and *P. aeruginosa* colonies and destroy their biofilms while promoting hFOB viability up to 7 days in vitro both in the absence and presence of 0.4 T external magnetic field. Synthesized Ch – SPIONs were also demonstrated as a negative contrast agent for MRI. A potential application of Ch – SPIONs is to use them in bone infection treatments. The superparamagnetic properties of Ch – SPIONs will allow them to be targeted to the infected bone tissue, and the efficacy of targeting can be monitored with MRI. The most important outcome of this study is that Ch – SPIONs can fight with biofilm surrounding the tissues and yet, still promote bone cell viability even under the influence of external static magnetic field to target the nanoparticles.

That said, there are various limitations of the present study. For instance, typically a variety of bacteria strains, rather than a single strain, is present at an infection site. A potential test for the future can be in vitro assessment of the antibacterial activity of the nanoparticle composites with microbial co-cultures to better mimic the biofilm occurring in the body. In addition, the amount of chitosan in the composite nanoparticle might be increased to provide enhanced antibacterial activity against gram negative bacteria. Moreover, in vivo animal experiments should also be conducted in the future to assess the performance of Ch – SPIONs under realistic infection scenarios and to better understand their biodistribution and clearance time of Ch – SPIONs from the body, which can potentially induce systemic problems, that is, allergies and toxicity. Despite all these unknowns, our preliminary proof of concept work showed great potential for the Ch – SPIONs to be used as a targeted antibacterial agent that can be monitored via MRI for bone infection.

4 | CONCLUSION

This study investigated the use of Ch – SPIONs synthesized in a microfluidic reactor for antibacterial applications. The obtained size of Ch – SPIONs was 8.8 ± 1.2 nm and particles showed superparamagnetic properties with a magnetization value of 32.0 emu/g. The colloidal stability of SPIONs in aqueous environment were improved by composite nanoparticle formation with chitosan, which made Ch – SPIONs a potential candidate as a negative contrast agent in MRI. hFOBs cultured with Ch – SPIONs less than 1 g/L concentration were viable and proliferated up to 7 days in vitro both in the presence and absence of a 0.4 T external static magnetic field. 0.5 g/L Ch – SPIONs, which promoted hFOB viability, reduced *S. aureus* growth by 63% and *P. aeruginosa* growth by 50% at 48 h of culture in vitro. Thus, Ch – SPIONs synthesized by a microfluidic device was shown to be a promising alternative to currently-used therapies to fight against infection.

ACKNOWLEDGMENTS

The authors would like to thank The Scientific Research Council of Turkey (Grant No: 117M187, 118M652 and 219M480), TÜBA (Outstanding Young Scientists Award, GEBİP) and Bilim Akademisi (Science Academy's Young Scientist Awards Program) for financial support. We would like to acknowledge Middle East Technical University (METU) Central Laboratory, BIOMATEN-METU Center of Excellence in Biomaterials and Tissue Engineering, and National Nanotechnology Research Center (UNAM) for fabricating the master mold, TEM, FTIR, VSM, TGA and zeta potential analysis. We also

would like to acknowledge Abdul Malik Wahab for fabrication of the master mold.

DATA AVAILABILITY STATEMENT

The data that support the findings of this study are available on request from the corresponding author. The data are not publicly available due to privacy or ethical restrictions.

ORCID

Melisa Kafali https://orcid.org/0000-0001-5306-7135
O. Berkay Şahinoğlu https://orcid.org/0000-0002-0984-9882
Yiğithan Tufan https://orcid.org/0000-0001-7549-8040
Z. Cemre Orsel https://orcid.org/0000-0001-5207-4325
Elif Aygun https://orcid.org/0000-0003-2934-6948
Beril Alyuz https://orcid.org/0000-0001-9172-1505
Emine Ulku Saritas https://orcid.org/0000-0001-8551-1077
E. Yegan Erdem https://orcid.org/0000-0001-9852-2293
Batur Ercan https://orcid.org/0000-0003-1657-1142

REFERENCES

1. Dulińska-Litewka J, Łazarczyk A, Hałubiec P, Szafrański O, Karnas K, Karewicz A. Superparamagnetic iron oxide nanoparticles—current and prospective medical applications. *Materials (Basel)*. 2019;12:617. doi: 10.3390/ma12040617
2. Mahmoudi M, Sant S, Wang B, Laurent S, Sen T. Superparamagnetic iron oxide nanoparticles (SPIONs): development, surface modification and applications in chemotherapy. *Adv Drug Deliv Rev*. 2011;63:24-46.
3. Suciu M, Ionescu CM, Ciorita A, et al. Applications of superparamagnetic iron oxide nanoparticles in drug and therapeutic delivery, and biotechnological advancements. *Beilstein J Nanotechnol*. 2020;11: 1092-1109.
4. Sun C, Lee JSH, Zhang M. Magnetic nanoparticles in MR imaging and drug delivery. *Adv Drug Deliv Rev*. 2008;60:1252-1265.
5. Alipour A, Soran-Erdem Z, Utkur M, et al. A new class of cubic SPIONs as a dual-mode T1 and T2 contrast agent for MRI. *Magn Reson Imaging*. 2018;49:16-24.
6. Vakili-Ghartavol R, Momtazi-Borojeni AA, Vakili-Ghartavol Z, et al. Toxicity assessment of superparamagnetic iron oxide nanoparticles in different tissues. *Artif Cells Nanomed Biotechnol*. 2020;48:443-451.
7. Thakor AS, Jokerst JV, Ghanouni P, Campbell JL, Mittra E, Gambhir SS. Clinically approved nanoparticle imaging agents. *J Nucl Med*. 2016;57:1833-1837.
8. James M, Revia RA, Stephen Z, Zhang M. Microfluidic synthesis of iron oxide nanoparticles. *Nanomaterials*. 2020;10:1-19.
9. Arakha M, Pal S, Samantarrai D, et al. Antimicrobial activity of iron oxide nanoparticle upon modulation of nanoparticle-bacteria interface. *Sci Rep*. 2015;5:1-12.
10. Baptista PV, McCusker MP, Carvalho A, et al. Nano-strategies to fight multidrug resistant bacteria—"a Battle of the titans". *Front Microbiol*. 2018;9:9.
11. Quan K, Zhang Z, Ren Y, et al. Homogeneous distribution of magnetic, antimicrobial-carrying nanoparticles through an infectious biofilm enhances biofilm-killing efficacy. *Sci Eng*. 2020;6:205-212.
12. Gokduman K, Bestepe F, Li L, Yarmush ML, Usta OB. Dose-, treatment- and time-dependent toxicity of superparamagnetic iron oxide nanoparticles on primary rat hepatocytes. *Nanomedicine*. 2018; 13:1267-1284.
13. Balk M, Haus T, Band J, et al. Cellular SPION uptake and toxicity in various head and neck cancer cell lines. *Nanomaterials*. 2021;11: 1-19.
14. Ghosh S, Ghosh I, Chakrabarti M, Mukherjee A. Genotoxicity and biocompatibility of superparamagnetic iron oxide nanoparticles: influence of surface modification on biodistribution, retention, DNA damage and oxidative stress. *Food Chem Toxicol*. 2020;136:110989.
15. Park W, Yang HN, Ling D, et al. Multi-modal transfection agent based on monodisperse magnetic nanoparticles for stem cell gene delivery and tracking. *Biomaterials*. 2014;35:7239-7247.
16. Wahajuddin and S. Arora. Superparamagnetic iron oxide nanoparticles: magnetic nanoplatforms as drug carriers. *Int J Nanomedicine*. 2012;7:3445-3471.
17. Li J, Zhuang S. Antibacterial activity of chitosan and its derivatives and their interaction mechanism with bacteria: current state and perspectives. *Eur Polym J*. 2020;138:109984.
18. Gadkari RR, Suwalka S, Yogi MR, Ali W, Das A, Alagirusamy R. Green synthesis of chitosan-cinnamaldehyde cross-linked nanoparticles: characterization and antibacterial activity. *Carbohydr Polym*. 2019; 226:115298.
19. Samrot AV, Sahithya CS, Selvarani J, Purayil ASK, Ponnaiah P. A review on synthesis, characterization and potential biological applications of superparamagnetic iron oxide nanoparticles. *Curr Res Green Sustain Chem*. 2021;4:100042.
20. Erdem EY, Cheng JC, Doyle FM, Pisano AP. Multi-temperature zone, droplet-based microreactor for increased temperature control in nanoparticle synthesis. *Small*. 2014;10:1076-1080.
21. Christopher GF, Anna SL. Microfluidic methods for generating continuous droplet streams. *J Phys D Appl Phys*. 2007;40:R319-R336. doi: 10.1088/0022-3727/40/19/R01
22. Niculescu AG, Chircov C, Bîrcă AC, Grumezescu AM. Nanomaterials synthesis through microfluidic methods: an updated overview. *Nanomaterials*. 2021;11:864. doi:10.3390/nano11040864
23. Frenz L, El Harrak A, Pauly M, Bégin-Colin S, Griffiths AD, Baret JC. Droplet-based microreactors for the synthesis of magnetic iron oxide nanoparticles. *Angew Chem Int Ed*. 2008;47:6817-6820.
24. Ahrberg CD, Choi JW, Chung BG. Droplet-based synthesis of homogeneous magnetic iron oxide nanoparticles. *Beilstein J Nanotechnol*. 2018;9:2413-2420.
25. Abdul Wahab M, Erdem EY. Multi-step microfludic reactor for the synthesis of hybrid nanoparticles. *J Micromech Microeng*. 2020;30: 1-10.
26. Abou-hassan A, Sandre O, Cabuil V, Abou-hassan A, Sandre O, Cabuil V. Microfluidics for the Synthesis of Iron Oxide Nanoparticles. 2019.
27. Wiegand I, Hilpert K, Hancock REW. Agar and broth dilution methods to determine the minimal inhibitory concentration (MIC) of antimicrobial substances. *Nat Protoc*. 2008;3:163-175.
28. Freire TM, Dutra LMU, Queiroz DC, et al. Fast ultrasound assisted synthesis of chitosan-based magnetite nanocomposites as a modified electrode sensor. *Carbohydr Polym*. 2016;151:760-769.
29. Zhang L, Chen Q, Ma Y, Sun J. Microfluidic methods for fabrication and engineering of nanoparticle drug delivery systems. *ACS Appl Bio Mater*. 2020;3:107-120.
30. Wang J, Song Y. Single molecule force spectroscopy to compare natural versus artificial antibody–antigen interaction. *Small*. 2017;13:1-19.
31. S Informat Mater Sci, 2010; 1–9.
32. Zhao G, Wang J, Peng X, Li Y, Yuan X, Ma Y. Facile solvothermal synthesis of mesostructured Fe_3O_4/chitosan nanoparticles as delivery vehicles for pH-responsive drug delivery and magnetic resonance imaging contrast agents. *Chem Asian J*. 2014;9:546-553.
33. Yasmeen S, Kabiraz M, Saha B, Qadir M, Gafur M, Masum S. Chromium (VI) ions removal from tannery effluent using chitosan-microcrystalline cellulose composite as adsorbent. *Int Res J Pure Appl Chem*. 2016;10:1-14.
34. Queiroz MF, Melo KRT, Sabry DA, Sassaki GL, Rocha HAO. Does the use of chitosan contribute to oxalate kidney stone formation? *Mar Drugs*. 2015;13:141-158.

35. Saber Braim F, Razak NNANA, Aziz AA, Ismael LQ, Sodipo BK. Ultrasound assisted chitosan coated iron oxide nanoparticles: influence of ultrasonic irradiation on the crystallinity, stability, toxicity and magnetization of the functionalized nanoparticles. *Ultrason Sonochem*. 2022;88:106072.
36. Ziegler-Borowska M, Chełminiak D, Kaczmarek H. Thermal stability of magnetic nanoparticles coated by blends of modified chitosan and poly(quaternary ammonium) salt. *J Therm Anal Calorim*. 2015;119:499-506.
37. Marroquin JB, Rhee KY, Park SJ. Chitosan nanocomposite films: enhanced electrical conductivity, thermal stability, and mechanical properties. *Carbohydr Polym*. 2013;92:1783-1791.
38. Mohammadi-Samani S, Miri R, Salmanpour M, Khalighian N, Sotoudeh S, Erfani N. Preparation and assessment of chitosan-coated superparamagnetic Fe_3O_4 nanoparticles for controlled delivery of methotrexate. *Res Pharm Sci*. 2013;8:25-33.
39. Zhu A, Yuan L, Liao T. Suspension of Fe_3O_4 nanoparticles stabilized by chitosan and o-carboxymethylchitosan. *Int J Pharm*. 2008;350:361-368.
40. Thangudu S, Huang EY, Su CH. Safe magnetic resonance imaging on biocompatible nanoformulations. *Biomater Sci*. 2022;10:5032-5053. doi:10.1039/d2bm00692h
41. Li X, Lu S, Xiong Z, et al. Light-addressable nanoclusters of Ultrasmall iron oxide nanoparticles for enhanced and dynamic magnetic resonance imaging of arthritis. *Adv Sci*. 2019;6:1-9.
42. Arsalani S, Guidelli EJ, Silveira MA, et al. Magnetic Fe3O4 nanoparticles coated by natural rubber latex as MRI contrast agent. *J Magn Magn Mater*. 2019;475:458-464.
43. Stephen ZR, Kievit FM, Zhang M. Magnetic resonance biomarkers in radiation oncology. *Mater Today (Kidlington)*. 2011;23:1-7.
44. Taşar C, Ercan B. Fabrication and biological properties of magnetic bioactive glass nanoparticles. *Ceram Int*. 2023;49:12925-12933.
45. Sahariah P, Gaware VS, Lieder R, et al. The effect of substituent, degree of acetylation and positioning of the cationic charge on the antibacterial activity of quaternary chitosan derivatives. *Mar Drugs*. 2014;12:4635-4658.
46. Sibov TT, Pavon LF, Miyaki LA, et al. Umbilical cord mesenchymal stem cells labeled with multimodal iron oxide nanoparticles with fluorescent and magnetic properties: application for in vivo cell tracking. *Int J Nanomedicine*. 2014;9:337-350.
47. Miyakoshi J. Effects of static magnetic fields at the cellular level. *Prog Biophys Mol Biol*. 2005;87:213-223.
48. Wiskirchen J, Groenewaeller EF, Kehlbach R, et al. Long-term effects of repetitive exposure to a static magnetic field (1.5 T) on proliferation of human fetal lung fibroblasts. *Magn Reson Med*. 1999;41:464-468.
49. Yang J, Zhang J, Ding C, Dong D, Shang P. Regulation of osteoblast differentiation and iron content in MC3T3-E1 cells by static magnetic field with different intensities. *Biol Trace Elem Res*. 2018;184:214-225.
50. Seabra AB, Pelegrino MT, Haddad PS. Antimicrobial applications of superparamagnetic iron oxide nanoparticles. *Antimicrobial Applications of Superparamagnetic Iron Oxide Nanoparticles: Perspectives and Challenges*. Elsevier Inc.; 2017.
51. Nehra P, Chauhan RP, Garg N, Verma K. Antibacterial and antifungal activity of chitosan coated iron oxide nanoparticles. *Br J Biomed Sci*. 2018;75:13-18.
52. Chevalier S, Bouffartigues E, Bodilis J, et al. Structure, function and regulation of Pseudomonas aeruginosa porins. *FEMS Microbiol Rev*. 2017;41:698-722.
53. Mulani MS, Kamble EE, Kumkar SN, Tawre MS, Pardesi KR. Emerging strategies to combat ESKAPE pathogens in the era of antimicrobial resistance: a review. *Front. Microbiol*. 2019;10:539. doi:10.3389/fmicb.2019.00539
54. Karimi Jabali M, Allafchian AR, Jalali SAH, Shakeripour H, Mohammadinezhad R, Rahmani F. Design of a pDNA nanocarrier with ascorbic acid modified chitosan coated on superparamagnetic iron oxide nanoparticles for gene delivery. *Colloids Surf A Physicochem Eng Asp*. 2022;632:127743.

SUPPORTING INFORMATION

Additional supporting information can be found online in the Supporting Information section at the end of this article.

How to cite this article: Kafali M, Şahinoğlu OB, Tufan Y, et al. Antibacterial properties and osteoblast interactions of microfluidically synthesized chitosan – SPION composite nanoparticles. *J Biomed Mater Res*. 2023;111(11):1662-1677. doi:10.1002/jbm.a.37575